Journal of Nuclear Materials 436 (2013) 68–75
DOI: http://dx.doi.org/10.1016/j.jnucmat.2013.01.331

Microstructure and mechanical behavior of ODS and non-ODS Fe–14Cr model alloys produced by spark plasma sintering

M.A. Auger, V. de Castro, T. Leguey *, A. Muñoz, R. Pareja

Departamento de Física, Universidad Carlos III de Madrid, 28911 Leganés, Spain

Abstract: In this work the spark plasma sintering (SPS) technique has been explored as an alternative consolidation route for producing ultra-fine grained Fe–14Cr model alloys containing a dispersion of oxide nanoparti-cles. Elemental powders of Fe and Cr, and nanosized Y_2O_3 powder have been mechanically alloyed in a planetary ball mill and rapidly sintered in a spark plasma furnace. Two alloys, with nominal compositions Fe–14%Cr and Fe–14% Cr–0.3%Y_2O_3 (wt.%), have been fabricated and their microstructure and mechanical properties investigated. The results have been compared with those obtained for other powder metal-lurgy processed alloys of the same composition but consolidated by hot isostatic pressing. The SPS tech-nique under the present conditions has produced Fe–14Cr materials that apparently exhibit different microstructures yielding inferior mechanical properties than the counterpart material consolidated by hot isostatic pressing. Although the presence of a dispersion of Y-rich particles is evident, the oxide dis-persion strengthened (ODS) Fe–14Cr alloy consolidated by SPS exhibits poor tensile properties. The extensive decoration of the powder particle surfaces with Cr-rich precipitates and the residual porosity appear to be responsible for the impaired properties of this ODS alloy consolidated by SPS.

1. Introduction

Reduced activation ferritic/martensitic (F/M) and ferritic steels are being considered candidate materials for structural applications in future fusion reactors as well as in the next generation of nuclear fission reactors [1–3]. The severe environment in which these materials will work requires them to be highly resistant to high heat fluxes, irradiation damage, thermomechanical stresses and chemical erosion or corrosion. A nanosized dispersion of yttrium oxide in the steel matrix improves the mechanical strength, and the resistance to creep and irradiation induced swelling [4]. Presently, oxide dispersion strengthened reduced activation ferritic steels (ODS RAF steels) are the leading structural materials for nuclear applications under investigation in Europe, Japan and the US [1,5–7]. In order to develop these alloys with the demanded mechanical properties and radiation resistance, the manufacturing route still needs to be optimized.

ODS steels are usually produced by powder metallurgy techniques. A blend of either elemental powders or atomized steel powder is mechanically alloyed with yttrium oxide powder to obtain a homogenous dispersion of nanoparticles in the steel matrix. The mechanically alloyed powder is then consolidated at high temperatures and pressures to produce the bulk material. Afterwards different thermomechanical treatments are applied to optimize its microstructure and mechanical properties. In the consolidation step the processing temperatures are critical in order to retain the nanocrystalline structure generated during the mechanical alloying and to impede particle coarsening and grain growth [8–10].

Hot isostatic pressing (HIP) and hot extrusion (HE) are the most commonly used consolidation processes, but processing costs and anisotropic properties are issues to be considered. As a result, other production routes that could improve the properties of the resulting material are being explored. This is the case of the SPS technique. This technique produces very fast sintering rates applying simultaneously uniaxial pressure and direct current pulses of a very high intensity to a powder sample contained in a graphite die. The potential benefit of SPS, as compared to conventional consolidation techniques should be higher density, smaller grain size and cleaner grain boundaries [11]. This technique has been recently employed to consolidate different types of ODS steels [12–14]. The nanostructured character of these SPS steels has been demonstrated in the case of F/M ODS Fe–9Cr using transmission electron microscopy (TEM), atom probe tomography (APT) and small angle neutron scattering (SANS) [13], or TEM analyses in the case of the ferritic ODS Fe–14Cr–3W–0.2Ti alloy [14]. Nevertheless, a mechanical characterization of the ODS steels prepared by SPS has not been accomplished to the authors' knowledge, with the exception of

* Corresponding author. Address: Departamento de Física, Universidad Carlos III de Madrid, Avda. Universidad, 30, 28911 Leganés, Madrid, Spain. Tel.: +34 916249448; fax: +34 916248749.

E-mail address: leguey@fis.uc3m.es (T. Leguey).

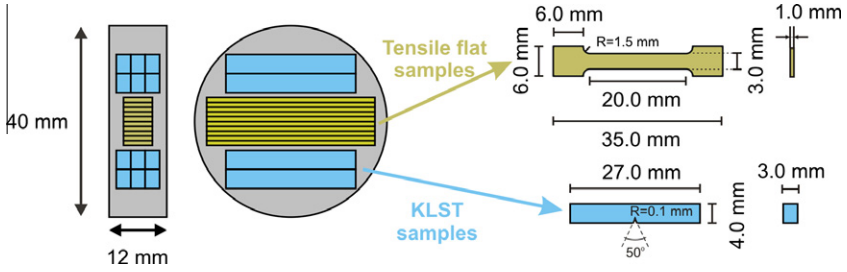

Fig. 1. Sketch showing the position, shape and dimensions of the samples cut from the alloy disks for the mechanical tests.

Table 1
Measured densities, microhardness values (*HV*), carbon and oxygen content for the model SPS alloys after being heat treated at 1123 K, and for the HIP alloys after being forged and subsequently heat treated at 1123 K.

	Milling atm.	ρ (g/cm^3)	*HV* (GPa)	C (wt.%)	O (wt.%)	Ref.
SPS Fe–14Cr	H	7.664 ± 0.002	1.74 ± 0.04	0.154 ± 0.014	0.329 ± 0.013	
SPS ODS	H	7.564 ± 0.002	2.76 ± 0.20	0.163 ± 0.001	0.384 ± 0.013	
HIP Fe–14Cr	He	7.654 ± 0.002	2.71 ± 0.04	0.07 ± 0.01	0.36 ± 0.01	[15]
HIP ODS1	He	7.711 ± 0.002	4.17 ± 0.05	0.05 ± 0.01	0.54 ± 0.11	[15]
HIP ODS2	H	7.48 ± 0.18	3.60 ± 0.08	0.03 ± 0.01	0.43 ± 0.04	[17]

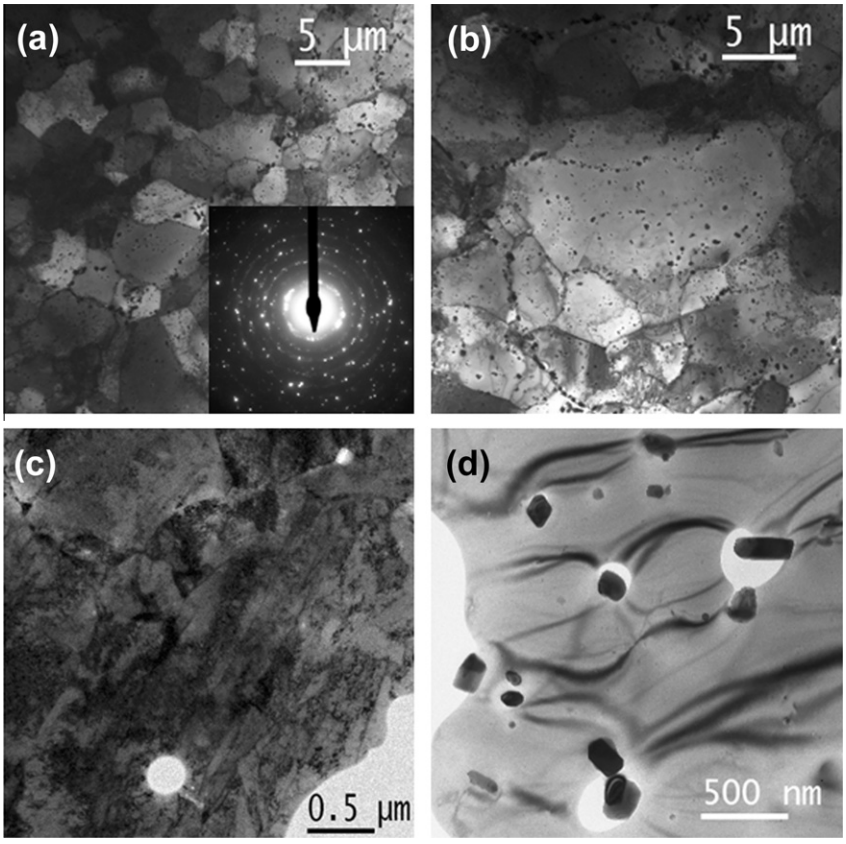

Fig. 2. Bright field TEM images of SPS Fe–14Cr. (a) Equiaxed grain structure; the inset shows a polycrystalline diffraction pattern. (b) Equiaxed grain structure and Cr-rich precipitates. (c) Lath structure. (d) Cr-rich precipitates.

the some exploratory tensile measurements at room temperature performed on austenitic Fe–17Cr–12Ni–2.5Mo–2.3Si and martensitic Fe–16Cr–2Ni [12], and on Fe–14Cr–3W–0.2Ti [14], which have not provided conclusive results.

The aim of this work is to assess the potential of the SPS technique for consolidation of ODS RAF steels processed by powder metallurgy. Two model ferritic alloys, with nominal compositions Fe–14%Cr and Fe–14%Cr–0.3%Y_2O_3 (wt.%), have been fabricated by mechanical alloying and SPS consolidation, and their microstructure, high temperature tensile properties and impact toughness investigated. The results have been compared with those obtained for other alloys of the same composition, milled under equivalent conditions, but consolidated by HIP and subsequent thermomechanical treatments [15–17].

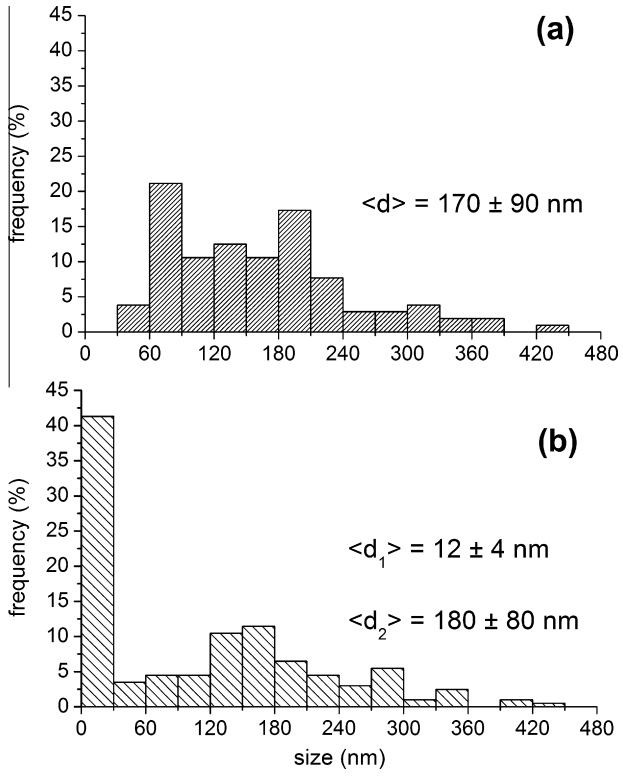

Fig. 3. Size distribution of Cr-rich and Y-rich particles for the SPS Fe–14Cr (a) and SPS ODS Fe–14Cr (b) alloys.

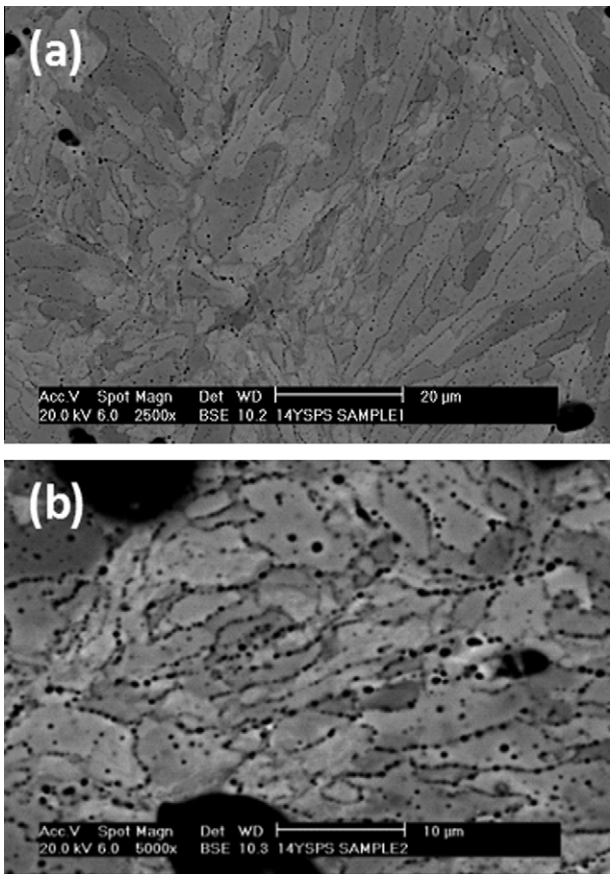

Fig. 5. BSE–SEM images of SPS ODS Fe–14Cr.

2. Experimental

Two alloys were prepared using as starting powders atomized 99.9% pure Fe and 99.5% pure Cr powders with particles sizes <10 μm, provided by Alfa Aesar, and 99.5% pure monoclinic Y_2O_3 spherical powder from nano-phase technologies with particle sizes <30 nm. Powder blends with target compositions: Fe–14%Cr and Fe–14%Cr–0.3%Y_2O_3 (wt.%), hereafter designed respectively as SPS Fe–14Cr and SPS ODS, were mechanically alloyed at 300 rpm for 60 h inside a chromium steel vessel (11–12%Cr) in a high-energy planetary mill (Fritsch Pulverisette 6) under a hydrogen atmosphere. Chromium steel balls (1–1.7%Cr, ∅10 mm) were used as grinding media with a ball-to-powder mass ratio of 10:1. The process of load and unload was carried out under an Ar atmosphere inside a glove box. More details on the chemical composition, particle morphology and size distribution of the mechanically alloyed powders can be found elsewhere [15].

SPS consolidation was carried out at FCT Systeme GmbH (Rauenstein, Germany) under vacuum using graphite dies. Disks of Ø40 mm and thickness ~12 mm were obtained after sintering for 4 min at 1373 K with an applied uniaxial pressure of 36 MPa. The density of the disks was evaluated using a He pycnometer and their Vickers microhardness measured using an applied load of 300 g for 20 s. Samples for tensile and Charpy impact tests were cut according to the diagram shown in Fig. 1, and heat treated for 1 h at 1123 K in vacuum followed by air cooling. The O and C contents were quantified using TC500 and CS600 LECO analyzers. Tensile tests were performed through the temperature range 295–973 K at a constant crosshead rate of 0.1 mm/min with the specimens un-der a flow of pure Ar. Charpy impact tests on KLST samples were also performed on both alloys from 173 K to 623 K.

The microstructure of the alloys was investigated using scanning electron microscopy (SEM) and TEM. A Philips XL30 scanning electron microscope equipped with an X-ray energy dispersive spectrometer (EDS) was used for the SEM analyses. TEM samples were prepared by electropolishing ∅3 mm disks in a TENUPOL 5 twin-jet polisher using 5%$HClO_4$ + 95%CH_3OH as electrolyte. The TEM and electron microdiffraction analyses were carried out in a Philips CM20 (S)TEM operated at 200 kV and equipped with an EDS system.

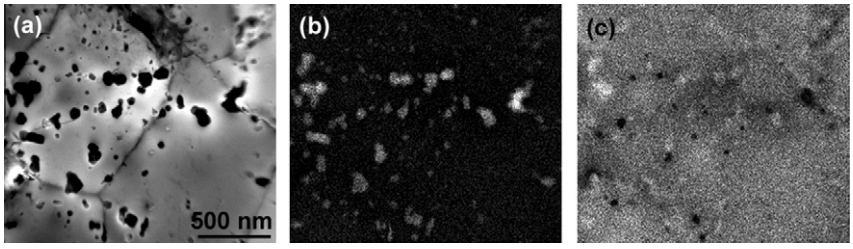

Fig. 4. (a) Bright field TEM image of SPS Fe–14Cr, and the elemental maps of the same region for (b) Cr and (c) Fe.

3. Results and discussion

3.1. Microhardness, density, and O and C content

Table 1 shows the density and the microhardness values measured for both alloys after the heat treatment at 1123 K. For comparison, results for counterpart alloys with the same composition and mechanical alloying procedure, but processed by HIP followed by forging and heat treated at 1123 K, are also presented. The following three alloys are included in the comparison: HIP Fe–14Cr, HIP ODS 1 and HIP ODS 2. These alloys were milled in helium or hydrogen, consolidated by HIP at 1373 K and 200 MPa for 2 h, forged at ~1350 K and finally heat treated at 1123 K [15,17]. The SPS Fe–14Cr alloy and its counterpart HIP alloy exhibit the same density but very different microhardness values, 1.74 GPa against 2.7 GPa. The same occurs for the SPS ODS alloy and the counterpart HIP ODS 2 alloy. The above indicate that the major contribution to the hardness of these materials should arise from the microstructural differences rather than residual porosity, although a higher density also appears to enhance the microhardness as the result for the HIP ODS 1 sample in comparison with the counterpart SPS ODS sample reveals. Nevertheless, it has to be elucidated in which extension the microhardness enhancement of the HIP samples, compared with the counterpart SPS samples, is due to forging or inherently to the HIP consolidation.

The C and O contents in the alloys are also indicated in Table 1. While all materials show similar values of O content, between 0.33 and 0.54 wt.%, the amount of C is significantly higher in the alloys produced by SPS (~0.16 wt.%) as compared to the material processed by HIP (0.03–0.07 wt.%). The high content in the SPS alloys is attributed to the diffusion of C from the graphite die during the sintering process.

3.2. Microstructure

3.2.1. SPS Fe–14Cr

The general microstructure of SPS Fe–14Cr is shown in the TEM images of Fig. 2. The grain structure consists of extensive areas of equiaxed grains <10 μm, with average sizes 5 ± 2 μm, together with some larger isolated grains, as Fig. 2a and b reveal. This grain structure appears to be more homogeneous than the one corresponding to the counterpart model Fe–14Cr alloy consolidated by HIP, which exhibited a bimodal structure consisting of areas comprising large equiaxed grains with sizes up to 7 μm, and regions containing submicron grains [15]. The polycrystalline diffraction patterns reveal that these areas exhibit an untextured bcc structure corresponding to the ferrite phase as shows the inset of Fig. 2a. It is interesting to notice that few regions of this SPS Fe–14Cr alloy exhibit a microstructure of martensite laths with widths of ~90 nm as Fig. 2c shows. Evidence of lath martensite was not detected in the counterpart HIP Fe–14Cr alloy. The formation of lath martensite in SPS Fe–14Cr is attributed to: (i) C intake from the graphite die and plugs of the SPS furnace, (ii) Cr depletion in the matrix due to formation of Cr-rich precipitates, and (iii) a fast cooling rate. It is known that C in the Fe–Cr system expands the γ loop to higher Cr content [18]. The C content in the HIP Fe–14Cr alloy, as well as in the HIP ODS samples, was <0.1 wt.%, see Table 1. The higher C content in the counterpart SPS materials could have made possible the accomplishment of the consolidation process

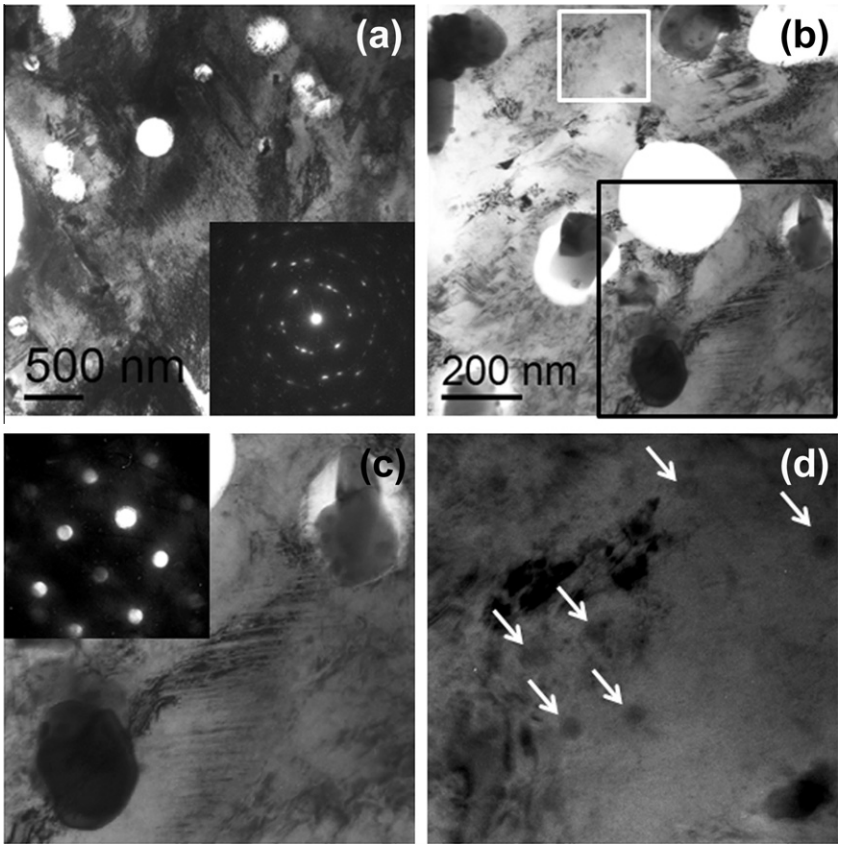

Fig. 6. Bright field TEM images of SPS ODS Fe–14Cr. (a) Subgrain and dislocation structure; the inset shows a polycrystalline diffraction pattern. (b) Distribution of Cr-rich precipitates. (c) Enlarged image of the region framed in black in image (b); the inset shows the microdiffraction pattern of the precipitate indexed as Cr_2O_3 in the [1 2 1] zone axis. (d) Enlarged image of the region framed in white in image (b); the Y-rich nanoparticles are pointed out by white arrows.

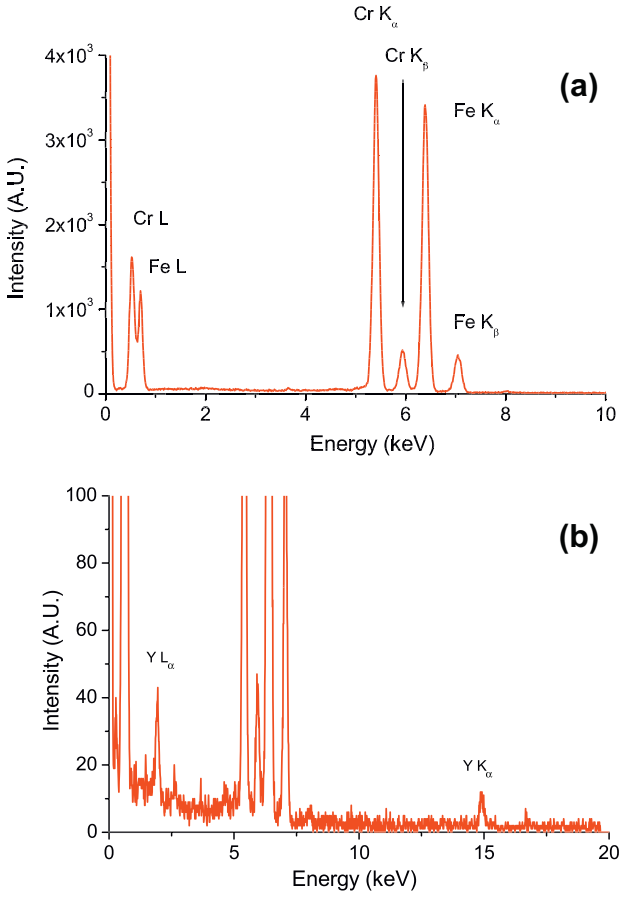

Fig. 7. EDS spectrum of (a) a Cr-rich precipitate and (b) a Y-rich nanoparticle in the SPS ODS Fe–14Cr alloy.

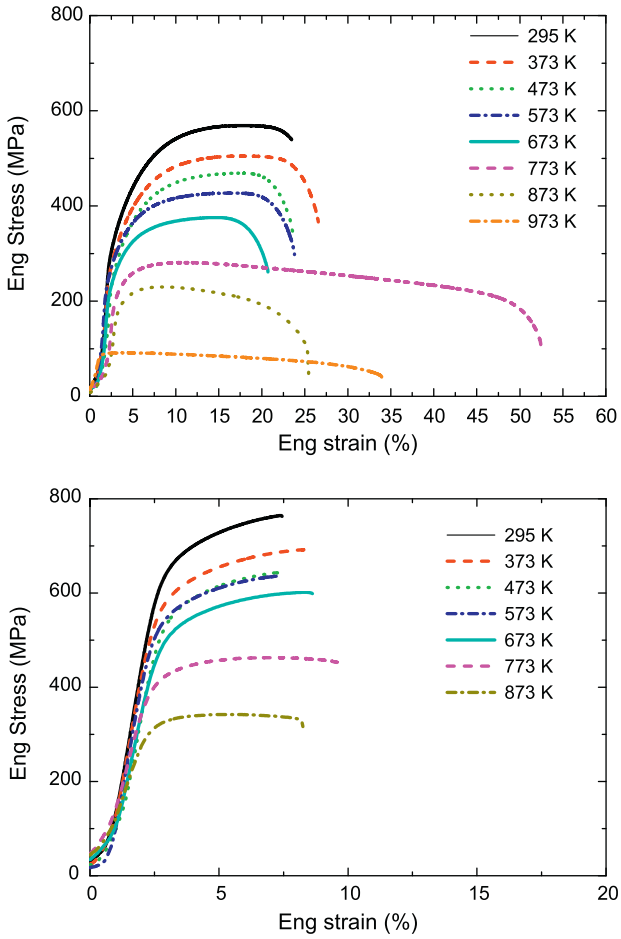

Fig. 8. Stress–strain curves at different test temperatures. (a) SPS Fe–14Cr. (b) SPS ODS Fe–14Cr.

in the γ or (γ + α) field that together with a faster cooling rate, may give rise to the formation of martensite in the SPS samples.

Precipitates with sizes ~40–500 nm are present in the alloy, see histogram in Fig. 3a. Most of them are seen distributed inside the grains, and they are sometimes found aligned or attached to other precipitates, as Figs. 2b and d show. These precipitates exhibit faceted habits that could occasionally be elongated. The EDS analyses reveal that these precipitates have a Cr-rich composition. Fig. 4 shows the bright field (BF)-STEM image of a region with small precipitates together with the corresponding EDS elemental mapping image confirming the Cr enrichment in these secondary phases. Their crystalline structure was determined analyzing different electron microdiffraction patterns. Some of them could be identified as chromium carbides ($Cr_{23}C_6$ type), while others were identified as chromium oxides corresponding to the corundum structure (Cr_2O_3). These precipitates have very similar characteristics to the Cr-rich particles that were also found in the HIP Fe–14Cr alloy [15].

3.2.2. SPS ODS Fe–14Cr

Backscattered electron (BSE) SEM images of electropolished samples are shown in Fig. 5. A structure of elongated aspect is apparent. Although it seems to be composed of long thin grains with average size 7 ± 4 μm and lengths up to ~30 μm in the SEM images, it is very likely a reflection of the morphology and size of the prior milled powder particles. Their boundaries appear decorated with Cr-rich precipitates as shown in Fig. 5b. The TEM observations confirm that the elongated structure consists of a fine-grained substructure. Fig. 5 also reveals the presence of some holes with sizes up to ~10 μm that can be due to either residual porosity or large precipitates detached by the polishing process.

TEM micrographs of SPS ODS Fe–14Cr can be seen in Fig. 6. The grains appear to be composed of subgrains containing a high density of entangled dislocations as the TEM image and polycrystalline SAED pattern of Fig. 6a reveal. TEM images in Fig. 6a and b also show a non-negligible amount of holes re-vealed by the white circles, attributable to either detached pre-cipitates or close porosity. The second possibility would explain the lower density value measured for this alloy. Precipitates having a similar size distribution as compared to the non-ODS alloy, frequently faceted, are present, see Figs. 3b and 6b, c. As in the SPS Fe–14Cr, many of them are found decorating grain boundaries, and others inside the grains or agglomerated. More-over, these precipitates are Cr-rich as the EDS spectrum of Fig. 7a shows. The crystalline structure of some of them has also been determined from microdiffraction patterns, see for instance the pattern in Fig. 6b that could be indexed as Cr_2O_3 in the [12 1] zone axis. Dislocation cells and fine martensite laths are also visible in Fig. 6a and c. A high density of dislocations was also evident in the HIP ODS alloys, which had a fully fer-ritic submicron sized grain structure [15,17].

Besides the above Cr-rich precipitates, spherical particles with sizes <30 nm and average diameters of 12 ± 4 nm, such as the ones marked with white arrows in Fig. 6d, are found rather uniformly distributed inside the grains. EDS analyses confirmed that they are Y-rich particles, as the spectrum of Fig. 7b shows.

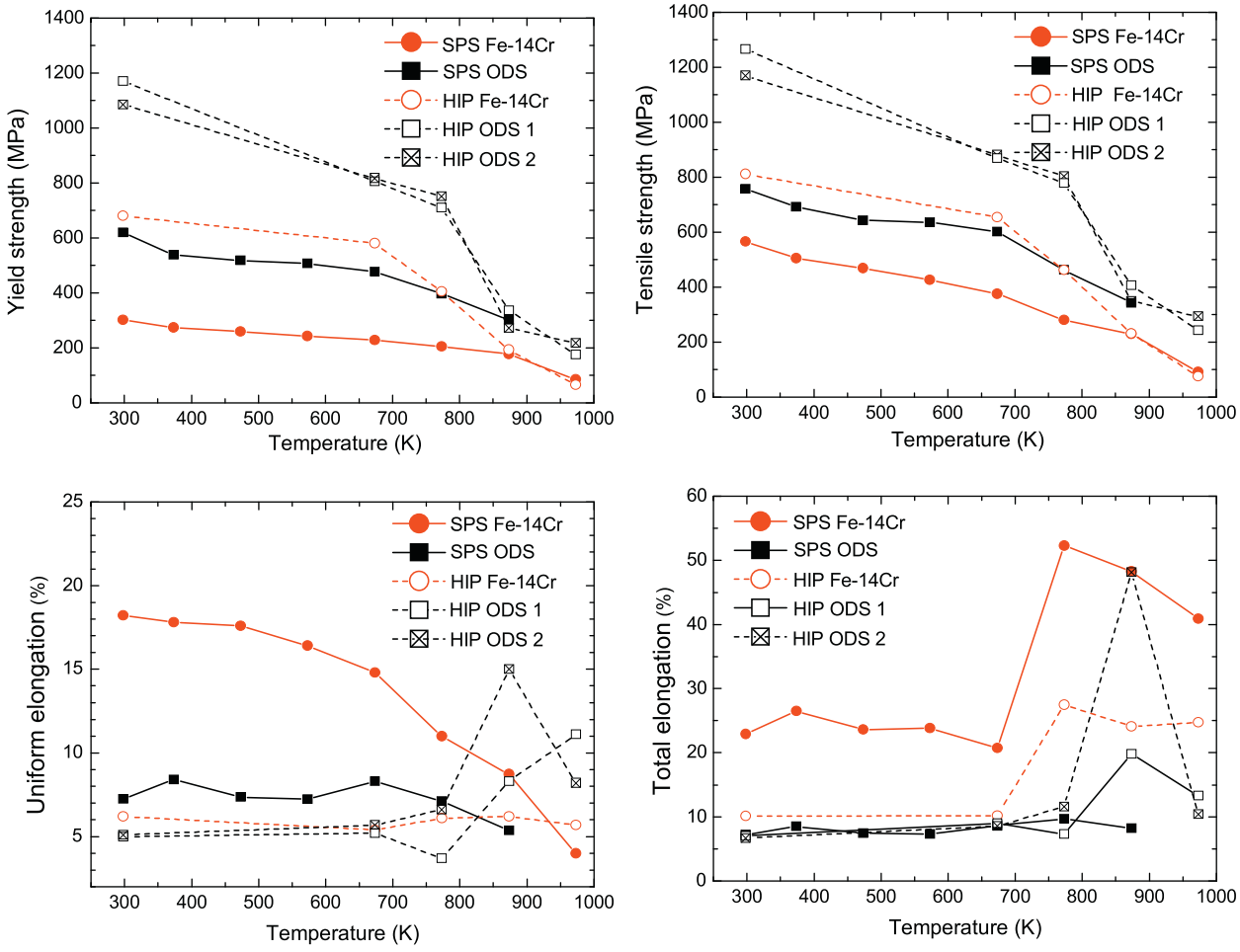

Fig. 9. Tensile properties as function of test temperature for the SPS Fe–14Cr and the SPS ODS alloys, and the counterpart HIP alloys studied in Refs. [11,12].

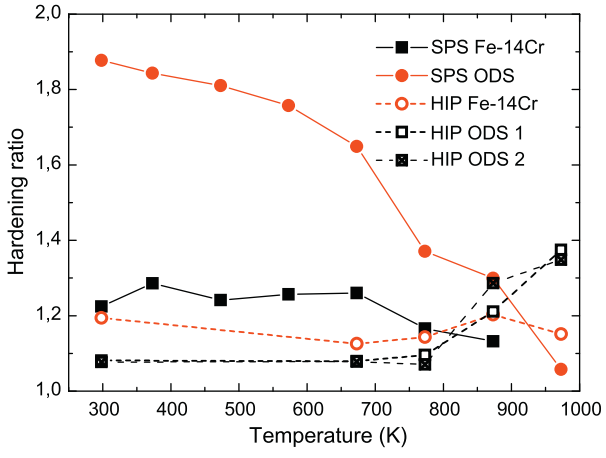

Fig. 10. Hardening ratio as a function of temperature for the SPS Fe–14Cr and the SPS ODS alloys, and the counterpart HIP alloys studied in Refs. [11,12].

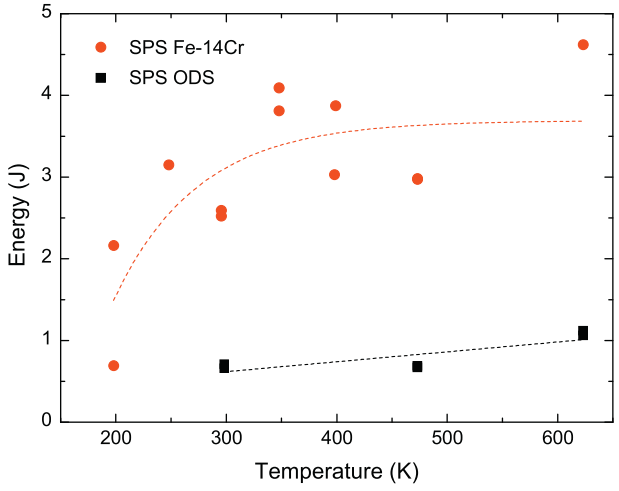

Fig. 11. Charpy impact energy as function of temperature for the SPS Fe–14Cr and the SPS ODS alloys.

3.3. Mechanical properties

3.3.1. Tensile results

Nominal stress–strain curves as function of temperature are represented in Fig. 8. The SPS Fe–14Cr alloy shows a wide plastic zone with a uniform elongation higher than 15% at temperatures <773 K. In contrast, the ODS counterpart alloy exhibits brittle behavior. In Fig. 9 the tensile properties for both alloys are summarized along with those for the counterpart HIP alloys studied in Refs. [15,17] for comparison. Yield strength values are defined as the stresses corresponding to a plastic deformation of 0.2%. Ultimate tensile strength values are referred to as tensile strength. The strengthening effect of the Y-rich nanoparticles in the SPS

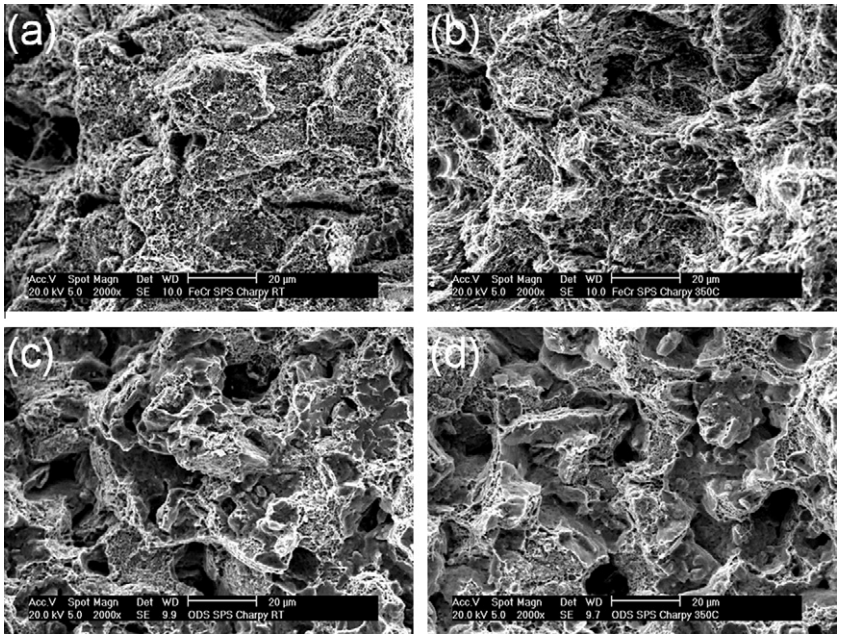

Fig. 12. SEM images of fractures surfaces after impact tests. (a) SPS Fe–14Cr tested at room temperature, (b) SPS Fe–14Cr tested at 623 K, (c) SPS ODS Fe–14Cr tested at room temperature, (d) SPS ODS Fe–14Cr tested at 623 K.

ODS alloy is evident in the yield strength and tensile strength values for the whole temperature range, see Fig. 9a and b. The yield strength increment respect to that for the Fe–14Cr alloy is maintained constant at ~250 MPa up to 700 K, and then it gradually starts to diminish. The yield and tensile strength values for the SPS alloys are noticeably lower than the corresponding values for the counterpart HIP alloys at temperatures <873 K. At temperatures $\geqslant$873 K both strengths for the ODS and non-ODS alloys separately converge irrespective of the consolidation technique. Regarding ductility, Fig. 9c and d shows the uniform and total elongation values. The values obtained for SPS Fe–14Cr are higher than for the SPS ODS alloy, although this effect decreases with increasing temperature above 673 K. The SPS ODS alloy exhibits uniform elongation values significantly higher than the HIP ODS alloys up to 773 K, while the total elongation remains constant and equal for the three ODS alloys, see Fig. 9c and d. This situation reverses above 773 K where the uniform elongation of the HIP ODS alloys increases steeply. All the alloys, except the SPS ODS one, exhibit a sharp increase in the total elongation values at these temperatures. This effect on the elongation of the ODS steels have also been reported by other authors [19,20].

Fig. 10 shows the hardening ratio, defined as the tensile strength/yield strength relation for the five alloys. The SPS materials exhibit higher hardening ratios than the counterpart HIP ones at temperatures <873 K. It is worthwhile to notice that the hardening ratios are particularly high for the SPS non-ODS alloy, and temperature decreasing. In contrast, the HIP ODS alloys exhibit an increase of the hardening ratio at temperatures >773 K.

3.3.2. Charpy impact results

The Charpy impact measurements for the SPS alloys are depicted as a function of temperature in Fig. 11. The SPS ODS alloy exhibits brittle behavior through the temperature range investigated, which can in principle be attributed to the residual porosity observed in this material and impairment of the intergranular cohesion due to decoration with Cr-rich particles. On the contrary, the SPS non-ODS alloy has upper shelf energy of ~3.5 J suggesting a DBTT that may be below room temperature. Complete impact curves have not be accomplished because of material shortage.

Fractographic examinations were carried out after the impact tests. Images of the fracture surfaces for the tests performed at RT and 350 °C are shown in Fig. 12. The SPS Fe–14Cr alloy presents mixed fracture modes at both temperatures. Cleavage is dominant at RT although dimples are also present, as Fig. 12a reveals. The ductile behavior becomes more important at higher temperatures, see Fig. 12b. The SPS ODS alloy exhibits brittle fracture in the whole temperature range investigated as it can be seen in Fig. 12c and d. Grain boundary decohesion appears to be the main fracture mechanism operating. This decohesion would be favored by the intergranular decoration with Cr-rich precipitates and the residual porosity present in this material.

4. Conclusions

The ODS Fe–14Cr and non-ODS Fe–14Cr alloys have been produced by powder metallurgy and consolidation by the SPS technique. Their microstructure, and tensile and Charpy impact properties have been investigated and the results compared with those reported for the counterpart alloys produced by HIP. It can be concluded the following:

1. The SPS technique under the present conditions has produced Fe–14Cr materials that apparently exhibit impaired microstructures yielding inferior mechanical properties than the counterpart material consolidated by HIP.
2. Although the presence of a dispersion of Y-rich particles is evident, the SPS ODS Fe–14Cr alloy exhibits brittle behavior, and microhardness and tensile properties comparable to the non-ODS alloys consolidated by HIP.
3. The extensive intergranular decoration of with Cr-rich particles and the residual porosity detected in the SPS ODS Fe–14Cr alloy appear to have deleterious effects on the mechanical properties.
4. An undesirable fraction of martensite has been detected in these SPS Fe–14Cr alloys attributable to C contamination from the SPS furnace device and Cr depletion in the inner of the grains, together with the inherent fast cooling rate of the SPS technique.

5. The effect of the SPS conditions on the microstructure control of the material have to be investigated in order to evaluate the potential of the SPS technique for producing ODS alloys with enhanced properties.

Acknowledgments

This investigation was supported by the Ministry of Science and Innovation of Spain (Project No. ENE 2008-06403-C06-04), the Comunidad de Madrid through the program ESTRUMAT-CM (Grant No. S0505/MAT/0077), and the European Commission through the European Fusion Development Agreement (Contract No. 09-240), the IP3 FP6 ESTEEM project (Contract No. 026019) and the Fusion Energy Materials Science (FEMaS) FP7 coordination action. The authors gratefully acknowledge the support of FCT Systeme GmbH for sintering the SPS alloys.

References

[1] D.T. Hoelzer, J. Bentley, M.A. Sokolov, M.K. Miller, G.R. Odette, M.J. Alinger, J. Nucl. Mater. 367–370 (2007) 166–172.
[2] P. Yvon, F. Carré, J. Nucl. Mater. 385 (2009) 217–222.
[3] I. Charit, K.L. Murty, JOM 62 (2010) 67–74.
[4] G.R. Odette, M.J. Alinger, B.D. Wirth, Ann. Rev. Mater. Res. 38 (2008) 471–503.
[5] N. Baluc et al., J. Nucl. Mater. 417 (2011) 149–153.
[6] H. Zhu, T. Wei, R. Harrison, L. Edwards, K. Maruyama, Eng. Asset Manage. Inf. Sustain. (2012) 1147–1160.
[7] A. Kimura, R. Kasada, A. Kohyama, H. Tanigawa, T. Hirose, K. Shiba, S. Jitsukawa, S. Ohtsuka, S. Ukai, M.A. Sokolov, R.L. Klueh, T. Yamamoto, G.R. Odette, J. Nucl. Mater. 367–370 (2007) 60–67.
[8] M.J. Alinger, G.R. Odette, D.T. Hoelzer, Acta Mater. 57 (2009) 392–406.
[9] P. Unifantowicz, Z. Oksiuta, P. Olier, Y. de Carlan, N. Baluc, Fus. Eng. Des. 86 (2011) 2413–2416.
[10] Z. Oksiuta, N. Baluc, Nucl. Fusion 49 (055003) (2009) 1–9.
[11] Z.A. Munir, U. Anselmi-Tamburini, M. Ohyanagi, J. Mater. Sci. 41 (2006) 763–777.
[12] Cs. Balázsi, F. Gillemot, M. Horváth, F. Wéber, K. Balázsi, F. Cinar Sahin, Y. Onüralp, A. Horváth, J. Mater. Sci. 46 (2011) 4598–4605.
[13] C. Heintze, M. Hernández-Mayoral, A. Ulbricht, F. Bergner, A. Shariq, T. Weissgärber, H. Frielinghaus, J. Nucl. Mater. 428 (2012) 139–146.
[14] Q.X. Sun, T. Zhang, X.P. Wang, Q.F. Fang, T. Hao, C.S. Liu, J. Nucl. Mater. 424 (2012) 279–284.
[15] M.A. Auger, T. Leguey, A. Muñoz, M.A. Monge, V. de Castro, P. Fernández, G. Garcés, R. Pareja, J. Nucl. Mater. 417 (2011) 213–216.
[16] V. de Castro, T. Leguey, M.A. Auger, S. Lozano-Perez, M.L. Jenkins, Nucl. Mater. 417 (2011) 217–220.
[17] M.A. Auger, V. de Castro, T. Leguey, M.A. Monge, A. Muñoz, R. Pareja, J. Nucl. Mater., in press. http://dx.doi.org/10.1016/j.jnucmat.2012.11.001.
[18] G.V Raynov, V.G Rivlin, Phase Equilibria in Iron Ternary Alloys, The Institute of Metals, London, 1988.
[19] P. Olier, A. Bougault, A. Alamo, Y. de Carlan, J. Nucl. Mater. 386–388 (2009) 561–563.
[20] R. Klueh, P.J. Maziasz, I.S. Kim, L. Heatherly, D.T. Hoelzer, N. Hashimoto, E.A. Kenik, K. Miyahara, J. Nucl. Mater. 307–311 (2002) 773–777.